Assessment of RISAT-1 and Radarsat-2 for Sea Ice Observations from a Hybrid-Polarity Perspective

Martine M. Espeseth *, Camilla Brekke and A. Malin Johansson (iD)

Department of Physics and Technology, UiT The Arctic University of Norway, 9019 Tromsø, Norway;
camilla.brekke@uit.no (C.B.); malin.johansson@uit.no (A.M.J.)
* Correspondence: martine.espeseth@uit.no; Tel.: +47-77645186

Abstract: Utilizing several Synthetic Aperture Radar (SAR) missions will provide a data set with higher temporal resolution. It is of great importance to understand the difference between various available sensors and polarization modes and to consider how to homogenize the data sets for a following combined analysis. In this study, a uniform and consistent analysis across different SAR missions is carried out. Three pairs of overlapping hybrid- and full-polarimetric C-band SAR scenes from the Radar Imaging Satellite-1 (RISAT-1) and Radarsat-2 satellites are used. The overlapping Radarsat-2 and RISAT-1 scenes are taken close in time, with a relatively similar incidence angle covering sea ice in the Fram Strait and Northeast Greenland in September 2015. The main objective of this study is to identify the similarities and dissimilarities between a simulated and a real hybrid-polarity (HP) SAR system. The similarities and dissimilarities between the two sensors are evaluated using 13 HP features. The results indicate a similar separability between the sea ice types identified within the real HP system in RISAT-1 and the simulated HP system from Radarsat-2. The HP features that are sensitive to surface scattering and depolarization due to volume scattering showed great potential for separating various sea ice types. A subset of features (the second parameter in the Stokes vector, the ratio between the HP intensity coefficients, and the α_s angle) were affected by the non-circularity property of the transmitted wave in the simulated HP system across all the scene pairs. Overall, the best features, showing high separability between various sea ice types and which are invariant to the non-circularity property of the transmitted wave, are the intensity coefficients from the right-hand circular transmit and the linear horizontal receive channel and the right-hand circular on both the transmit and the receive channel, and the first parameter in the Stokes vector.

Keywords: synthetic aperture radar; multi-sensor; full-polarimetry; hybrid-polarity; sea ice

1. Introduction

Synthetic Aperture Radar (SAR) has been widely used for sea ice observation for many years [1,2]. Due to the large Arctic area to cover, sea ice monitoring has primarily relied on single- and dual-polarization SAR scenes. In the Arctic, the SAR instrument is of special importance due its ability to monitor the Earth's surface independent of sun and weather conditions. The capabilities of full-polarimetric (FP) SAR data has been used to improve the interpretability of sea ice classes and to extract information needed to make reliable and more accurate sea ice charts compared to single-polarization SAR data (see [3,4]). These ice charts may be used for example in the shipping, fishing, and oil industries. One drawback of the FP mode is the small spatial coverage compared to some single-polarization SAR modes. To enable both high spatial coverage and increased amount of polarimetric information, the compact polarimetry (CP) SAR mode was introduced [5]. The CP mode is in the coherent dual-polarization (DP) SAR group, where the choice of the polarization channels deviates from the conventional DP SAR. In [5], Raney suggested the hybrid-polarity (HP) mode;

transmitting a right-hand circular (R) polarized signal while receiving in two orthogonal coherent linear vertical (V) and horizontal (H) polarized channels. The HP mode has the advantages of simpler instruments and of improving the quality of the radar measurements in terms of minimizing sensitivity to crosstalk, simpler calibration of the radar signals, and decreased on-board resource requirements [5]. The HP mode is already integrated in recent/current satellite missions such as the Radar Imaging Satellite-1 (RISAT-1) and the Advanced Land Observing Satellite-2 (ALOS-2), and this configuration will also be present in the next Radarsat Constellation Mission [6].

Utilizing similarities between various polarization modes and sensors will enable a multi-sensor analysis resulting in enhanced information content in terms of coverage and sea ice observations. A larger area can be covered using two sensors compared to one. If the two sensors are operating in different polarization modes, for example FP and HP, an extended ice chart can be made using non-overlapping parts from each of the sensors' acquisitions if their relationship is known. In addition, a change detection procedure between two scenes with two different polarization modes can only be performed if the relationship between them is known. The aim of for this study is to identify this relationship between the Radarsat-2 (RS-2) FP and the RISAT-1 (RI-1) HP mode based on similarity and dissimilarity between the two polarization modes.

In this study we analyze the differences in polarimetric information content in three pairs of overlapping HP and FP SAR scenes from the RI-1 and RS-2 satellites, respectively. To enable a direct comparison between the RS-2 and RI-1 scenes, we simulate HP data from the RS-2 data. The scene pairs were acquired in relation to a sea ice field work campaign in the Fram Strait between August to September 2015. The campaign is a part of the Fram Strait Arctic Ocean Outflow Observatory and was hosted by the Norwegian Polar Institute, where, amongst other data, in-situ sea ice measurements were collected. In addition, the pairs have close to equal incidence angle spans, geographic overlap, and quasi-simultaneous time of acquisition.

Some previous studies for sea ice observation using SAR have simulated HP data from RS-2's FP mode (see e.g., [7–10]). The studies in [7–10] all investigated various polarimetric features extracted from a simulated HP system from RS-2. Moreover, Dabboor and Geldsetzer et al. [7,9] investigated the separability amongst various sea ice classes using a set of HP features, and both studies concluded with promising results on sea ice separability using compact polarimetry. The studies in [7–10] are all based on simulated HP data from RS-2, while in this study we compare both a real and a simulated HP system. However, one recent study (see [11]) used one of the RI-1 scenes in a neural network for sea ice classification. Singha et al. [11] investigated the relative performance of a set of HP features for distinguishing the sea ice classes that they labelled based on ice charts produced by the Danish meteorological institute. In addition, Singha et al. [11] classified the sea ice in one of the overlapping RS-2 and RI-1 pairs, and found approximately the same classification results for both sensors. Another way of using hybrid-polarity SAR data is through reconstruction of a pseudo quad-polarimetric covariance matrix [12]. Espeseth et al. [13] investigated various reconstruction methods for overlapping L- and C-band SAR covering Arctic sea ice, and discovered higher reconstruction accuracy for L-band compared to C-band. However, in this study we choose to evaluate the hybrid-polarity SAR data directly to avoid the scattering symmetry assumptions introduced in a reconstruction approach. Rao et al. [14] also investigated the differences between the two sensors (RI-1 and RS-2), but for sand, water, urban, and crop surfaces. Rao et al. [14] discovered that the RI-1 differed from RS-2 when comparing the backscattered intensity values for the various surfaces. Especially, a large difference (approximately 7–8 dB) was found for water and sand surfaces. They concluded that these differences were due to better calibration for RS-2 compared to RI-1, the non-circularity property of the transmitted wave, and high values of the noise-equivalent-sigma-zero (NESZ) of RI-1.

The main objective of this study is to identify the similarities and dissimilarities between a simulated and a real HP system. In addition, we investigate how the separability between sea ice classes are affected by the non-circularity of the transmitted wave. The objectives are addressed by using three overlapping RI-1 and RS-2 scene pairs with the focus to directly compare the two sensors

and their corresponding modes (HP and FP). This is achieved by first homogenizing the dataset in terms of projecting the scenes onto a common grid with equal resolution, and further evaluating the data set in three ways; (1) through a noise analysis, where the backscattered intensities from the regions of interest in the SAR scenes are compared to the NESZ for each of the two sensors; (2) investigations of various multipolarization features extracted from selected sea ice regions; (3) comparison of the correlation between the two sensors to understand the relationship between a simulated and a real HP system.

This article is organized as follows. Section 2 presents the study area and the SAR scenes used, Section 3 briefly discusses polarimetric SAR theory, and Section 4 contains the results and discussions. Section 5 concludes this study.

2. Study Area and Data

2.1. Study Area

The two study areas are located in the Fram Strait; the first at approximate position 78°47.5′N and 6°31.5′W, and the second near the lle-de-France area (Northeast coast of Greenland) at position 78°8.9′N and 16°33.5′W. A large overview of the locations of the scenes and the positions of the research vessel (R/V) Lance can be seen in the top map in Figure 1.
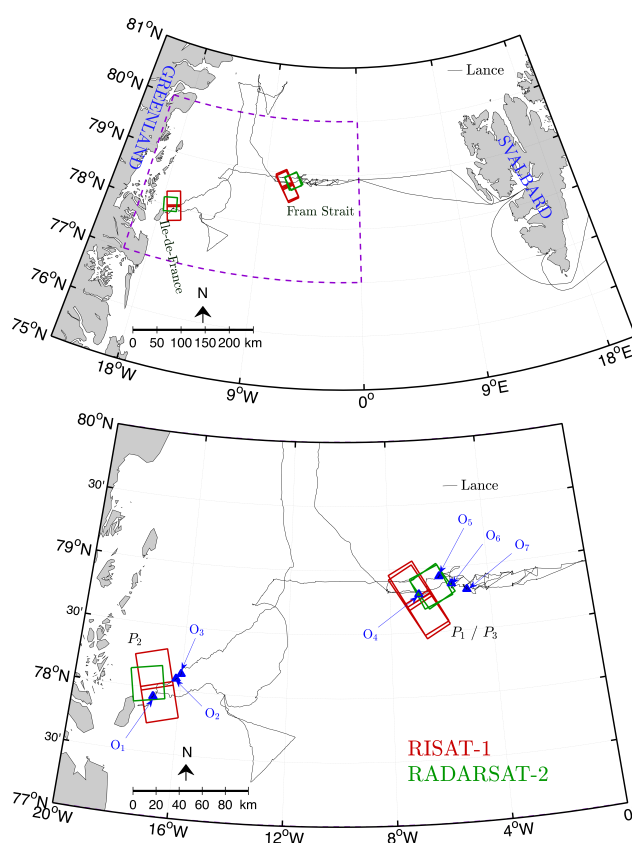
Figure 1. The top map shows the location of the scenes, R/V Lance's track positions (black lines), and the dashed purple square outlines the zoomed-in map on the bottom. The zoomed-in map shows marked areas on R/V Lance's track positions where relevant in-situ sea ice observations for this study were obtained.

The zoomed-in version (the bottom map) is the dashed purple square in the larger map. The zoomed-in version contains seven marked positions (indicated by an *O* symbol) and these positions

correspond to the relevant in-situ sea ice observations from ice stations for the SAR scenes used in this study. Note that several other in-situ observations were made, but we only highlight the ones relevant for this study. In Section 2.5, information from these positions is discussed and linked to the regions that are investigated in the SAR scenes.

2.2. Sensor Properties and the SAR Scenes

Sensor properties of the SAR modes investigated for RI-1 and RS-2 are presented in Table 1. RI-1 has higher NESZ than RS-2, which could, in general, be a disadvantage for identifying sea ice types with low backscattering, e.g., grease ice. RI-1, however, has spatially finer resolution than RS-2, which might be an advantage in identifying more detailed sea ice structure like narrow ridges and rafting patterns [15].

Table 1. Properties of the overlapping RISAT-1 (RI-1) [16] and Radarsat-2 (RS-2) scenes [17]. Both sensors transmit waves with frequency in the C-band region.

Pair	Satellite	Date	Time (UTC)	Polarization Mode (Beam)	Incidence Angle (Deg)	NESZ (dB)	Resolution (rg ^{a} × az ^{b}) (m)	Scene Size (km)	Time Diff. (min)	Overlap (km ^{2})	Distance (km) to Lance
P_1	RI-1	6 Sept.	16:38	HP (FRS-1)	26.0 to 28.4	−17	2 × 3	30 × 25	13	313	26
	RS-2	6 Sept.	16:55	FP (FQ-13)	32.5 to 34.0	−33.5 to −35.7	5.2 × 7.6	25 × 25			17
P_2	RI-1	6 Sept.	18:13	HP (FRS-1)	45.8 to 47.5	−17	2 × 3	30 × 25	22	582	287
	RS-2	6 Sept.	18:35	FP (FQ-29)	46.8 to 48.0	−31.4 to −32.6	5.2 × 7.6	25 × 25			291
P_3	RI-1	7 Sept.	16:30	HP (FRS-1)	22.5 to 24.8	−17	2 × 3	30 × 25	4	232	52
	RS-2	7 Sept.	16:26	FP (FQ-5)	23.4 to 25.3	−34.5 to −37.2	5.2 × 7.6	25 × 25			32

^{a} rg: slant range, ^{b} az: azimuth.

From Table 1, the images in scene pair #1 (P_1) are taken 13 min apart with low to intermediate incidence angles, while the scenes in pair #2 (P_2) have higher incidence angles and were taken 22 min apart. The scenes in the third pair (P_3) have low incidence angles and only 4 min between the acquisitions. The second last column of Table 1 gives the size of the overlapping area, while the last column contains the shortest distance between each of the scenes's bounding box and R/V Lance's position at acquisition time. In each pair, to obtain higher overlap to RS-2, there are two consecutive RI-1 scenes aligned in the azimuth direction (as seen in Figure 1). The two RI-1 scenes in each pair are merged to form one scene prior to the polarimetric analysis.

Figures 2–4 show the RS-2 and RI-1 scenes. The left-most image in Figures 2–4 is a red-green-blue (RGB) composite image (scaled for visual purposes), where the green band is the VV-intensity for RS-2, the red band is the RV-intensity from RI-1, and the blue band consist of only zero values. The overlapping area between the two sensors will then appear as yellow. The center image in Figures 2–4 is the RV-intensity from RI-1, while the right-most image is the VV-intensity from RS-2. The colorbar next to these intensity images are in decibel (dB). Note, the images in center and to the right show only the overlapping area (colored in yellow) in the RGB image.

2.3. SAR Pre-Processing

All the scenes are multi-looked and geo-coded such that each pixel covers approximately 8 × 8 m on the ground. The FRS-1 mode of RI-1 has finer resolution (almost doubled in range and azimuth direction compared to RS-2) and thus more pixels per ground cell compared to RS-2 (see Table 1). In order to get the same pixel spacing, more averaging is performed on the RI-1 products. The single look complex (SLC) products from both the RS-2 and RI-1 are converted to multi look complex (MLC) images and then projected on a spatial common grid with equal number of pixels on the ground. In addition, a co-registration (linear shift of the pixels in RS-2) is performed on the geo-coded products to adjust for the minor sea ice drift between the two scenes. Next, a 9 × 9 sliding window is applied on the geo-coded MLC RS-2 and RI-1 products. The latter procedure is mainly done in order to further reduce the speckle within the SAR scenes and to enhance interpretability [18]. The FRS-1 HP mode of

RI-1 represents a system where the right-hand circular is on transmit and linear horizontal and vertical polarizations are on receive.
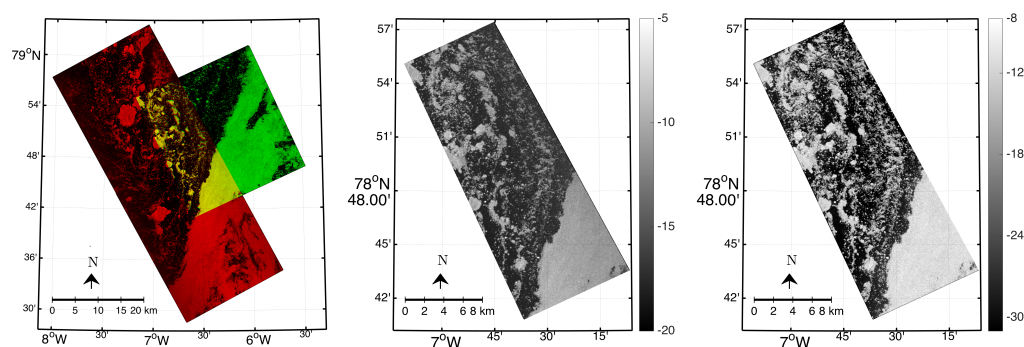
Figure 2. The left red-green-blue (RGB) composite image (scaled) of scene pair P_1, where the green band is the intensity of the linear vertical transmit and linear vertical receive channel (VV) from Radarsat-2 (RS-2) scene and red is the intensity of the right-hand circular transmit and vertical receive channel (RV) from RISAT-1 (RI-1) scene. Yellow indicates areas of overlap. The center (right) image is the RV (VV)-intensity of the overlapping area from RI-1 (RS-2). RS-2 Data and Products ©MDA LTD (2015)—All rights reserved. RI-1 ©2015-Antrix–All rights reserved.
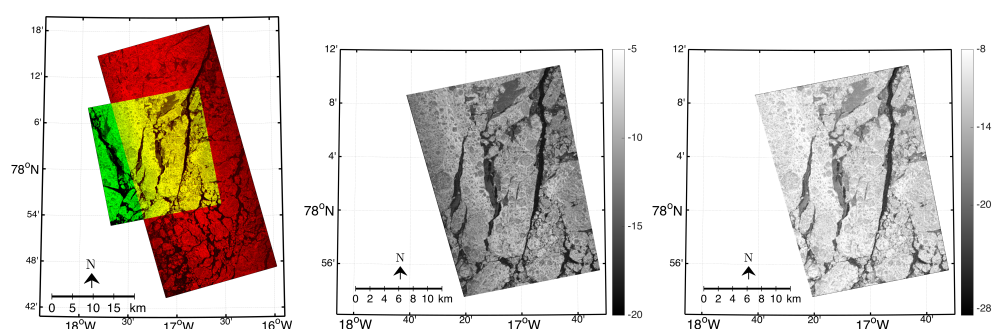
Figure 3. The left RGB image (scaled) of scene pair P_2, where the green band is the VV-intensity from RS-2 scene and red is the RV-intensity from RI-1 scene. Yellow indicates areas of overlap. The center (right) image is the RV (VV)-intensity of the overlapping area from RI-1 (RS-2). RS-2 Data and Products ©MDA LTD (2015)—All rights reserved. RI-1 ©2015-Antrix—All rights reserved.
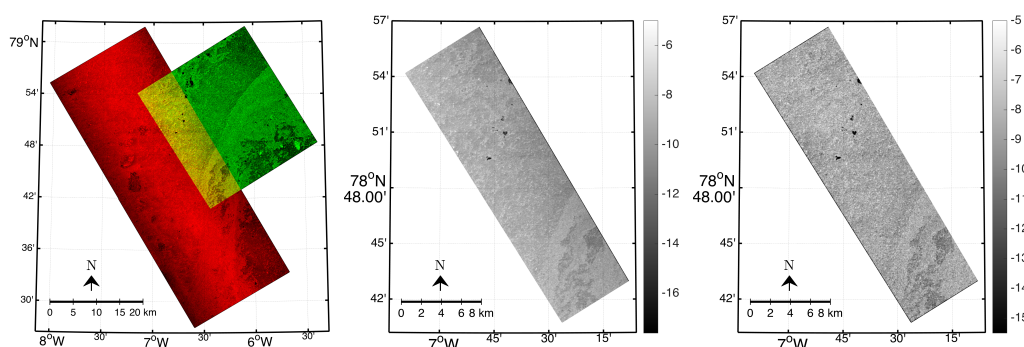
Figure 4. The left RGB image (scaled) of scene pair P_3, where the green band is the VV-intensity from RS-2 scene and red is the RV-intensity from RI-1 scene. Yellow indicates areas of overlap. The center (right) image is the RV (VV)-intensity of the overlapping area from RI-1 (RS-2). RS-2 Data and Products ©MDA LTD (2015)—All rights reserved. RI-1 ©2015-Antrix—All rights reserved.

2.4. Selection of ROIs and Profiles

We assume that no change has occurred in the sea ice properties between the scenes in each pair, justified by the small time difference. The investigated sea ice regions are manually selected using the intensities from both RI-1 and RS-2. The selection is based on finding regions of interest (ROIs) with varying intensity values. In addition, three profiles within each scene pair are selected for evaluation of the correlation between the two sensors. Figure 5 illustrates the ROIs investigated and the profiles, which are spatially equivalent for the RI-1 and RS-2 scenes. Figure 5 shows the ROIs overlaid the RI-1 scenes. Two sets of ROIs are selected for evaluation in P_1, four sets in P_2, and three sets in P_3; in total nine ROIs.
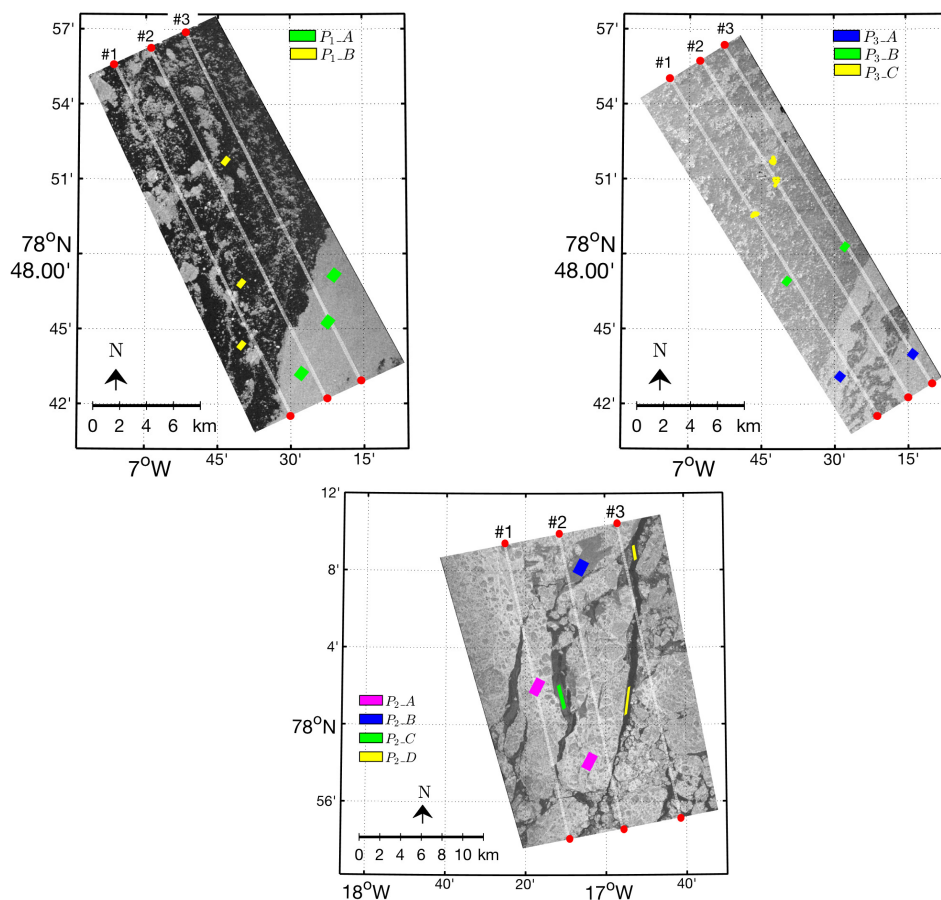
Figure 5. Illustrations of the regions of interest (ROIs) investigated. The ROIs are overlaid on top of RI-1 scenes for P_1 (**top left**), P_2 (**bottom**), and P_3 (**top right**). The profiles are indicated by light gray colored line between two red markers. The profiles are 50 pixels wide and passes through the azimuth direction.

2.5. In-Situ Information

The in-situ sea ice observations from dedicated ice stations near R/V Lance and some weather observations from the sea ice campaign are given in Table 2. This table is divided into two sections; one from the Ile-de-France area relevant for P_2; the second section from Fram Strait which is relevant for both P_1 and P_3. The scenes in P_2 are acquired close to the Ile-de-France area. Corresponding observations from R/V Lance were made 5 days prior to the P_2 acquisitions. Little change has occurred during these 5 days, which is confirmed by investigating two Sentinel-1 extra wide swath scenes, one from the day of the in-situ observations and one from the day of the two SAR acquisitions in P_2. The ice station observations from the Ile-de-France area are indicated by O_1, O_2, and O_3.

The observations showed varying sea ice types such as newly formed ice, nilas, leads, and thicker ice with snow cover. By investigating the SAR scenes and the observations, the selected ROIs are labelled as given in the right panel of Table 2.

Observations from R/V Lance in the area and close to the time of the acquisitions of P_1 and P_3 are given in the second section of Table 2 as O_4, O_5, O_6, and O_7. These observations showed scattered floes with thin ice (including frazil ice, grease ice, and nilas) up to 4 cm thick, and ice between 116–210 cm thick. In addition, the thin ice was often wet or covered with a very thin snow layer (<1 cm). Based on these observations and thickness measured the dark region named P_1_B is labelled as grease ice, while the brighter region P_1_A is labelled as first-year ice (FYI). The scenes in P_3 are acquired 24 h after P_1 at the same geographical position in the Fram Strait. The same observations from the P_1 area are also used when labelling the ROIs in P_3.

Some changes have occurred between P_1 and P_3 as can be seen in the intensity images in Figures 2 and 4. The temperature measured at the acquisition times (in vicinity of the two scenes in P_1, see last column in Table 1) of the scenes in P_1 was around 0 °C, while the temperature at acquisition times of the scenes in P_3 was around −2.5 °C. This gives a temperature drop of 2.5 °C. In addition, a small drop in relative humidity prior the acquisition of the scenes in P_3 was also measured between the two scenes. The effects from the temperature drop and reduction in relative humidity might have caused rime on the sea ice surface [19]. A new fresh snow layer between P_1 and P_3 was also seen during the on-board observations from ice stations near R/V Lance as indicated in the last row in Table 2 for O_7. These environmental factors might be the reasons for the different backscattering in the area covered by P_3 when compared to the same area the day before in P_1. Therefore, the ROIs P_3_A and P_3_B will most likely correspond to the same sea ice type defined for P_1_A and P_1_B, but with a new fresh snow layer. P_3_C is most likely melt ponds as these were also observed in the area. Note that the ice edge starting from the lower left corner across the intensity of the scenes in P_1 and P_3 is comparable.

Table 2. Overview of the in-situ observations (indicated by an *O* symbol) from sea ice stations near R/V Lance from the locations given in Figure 1. The right table shows the labelling of the ice types for the regions of interest (ROIs) investigated.

Area	ID	Date (Time) (UTC)	Observations	ROIs (Sea Ice Types)
Ile-de-France (P_2)	O_1	30.08 (22:19)	Newly formed ice and nilas (0.5–5 cm) with snow cover	P_2_A (FYI)
	O_2	31.08 (11:48)	Newly formed ice and nilas (0.5–4 cm) with snow cover	P_2_B (Flooded FYI) P_2_C (Nilas/newly formed ice with snow cover)
	O_3	31.08 (12:42)	Leads (2–3 cm), 110–235 cm thick ice and 5–8 cm snow cover	P_2_D (Leads)
Fram Strait (P_1 and P_3)	O_4	05.09 (11:20)	Scattered floes with 1–2 cm snow cover, melt ponds, and 137–210 cm thick ice	P_1_A (FYI) P_1_B (Grease/frazil ice)
	O_5	06.09 (07:25)	Newly formed frazil/ grease ice (3–4 cm)	
	O_6	06.09 (12:56)	High melt pond coverage, 2 cm snow, and 104–187 cm thick ice	P_3_A (FYI with fresh snow layer) P_3_B (Grease/frazil ice with fresh snow layer) P_3_C (Melt ponds)
	O_7	07.09 (07:42)	Snowfall, 3–4 cm fresh snow layer, and 116–130 cm thick ice	

3. Polarimetric Theory

The fundamental quantities measured by polarimetric SAR instruments are defined by the complex backscattering terms S_{ij}. Here, i and j are the polarizations of the transmit and receive channels in the radar system. The HP mode transmits only one circular polarization, either left (L) or right (R), and receives two orthogonal linear polarizations, namely horizontal and vertical [5]. The HP mode in RI-1 uses right circular transmit and linear horizontal and vertical receive. As pointed out by Touzi et al. [20], it is not possible to generate perfect circular polarization using current technology due to the phase errors in combining the horizontal and vertical with 90° phase difference when

transmitting circular waves. Therefore, the transmitted waves in the HP mode of RI-1 will be more elliptical rather than circular, hence the non-circularity property of RI-1 [14]. The ellipticity angle (χ) of the transmitted wave can be obtained from the axial ratio (AR), which defines the ratio between the major and minor axis from the electric field vector. The AR has been used in, e.g., [14,20] when discussing the non-circularity in general for a HP system. It is well known that an AR of 0 dB indicates perfect circular, while values above 0 dB corresponds to elliptical, and values of infinity is linear polarization [20].

According to the RI-1 design description the AR was given as 1.1 dB for RI-1, which gives ellipticity angle of 37.8° (see [14] and references therein). However, Rao et al. [14] estimated the AR (from corner reflectors) and further calculated the ellipticity angle to be of 43°. Note that a perfect circular wave has an ellipticity angle of ±45°. However, this value was estimated by considering a small range of incidence angles. As highlighted in [20], the non-circularity of the transmitted wave increases with incidence angle [21]. In this study, the simulated complex HP scattering vector is synthesized by considering an AR of 0 dB, which is defined as:

$$\bar{k}_{(RH,RV)} = [S_{RH}, S_{RV}]^T, \tag{1}$$

where T denotes the transpose operator. In addition, we also investigate a scattering vector having an ellipticity angle of $-38°$ (AR = 1.1 dB). By exploring this, we will be able to investigate the effect of the non-circularity of the transmitted wave in relation to sea ice separability. Note, both the simulated complex HP scattering vectors are generated from the FP RS-2 data. To the author's knowledge, the majority of the published studies investigating the capabilities of the HP mode does not have real HP data, and therefore need to simulate the HP data from the FP data, according to this relation (for AR = 0 dB):

$$\bar{k}_{(RH,RV)} = \frac{1}{\sqrt{2}}[S_{HH} - iS_{HV}, -iS_{VV} + S_{HV}]^T, \tag{2}$$

where reciprocity is assumed ($S_{HV} = S_{VH}$). The simulation of the HP with $\chi = -38°$ becomes [22]:

$$\bar{k}_{(RH,RV)} = [\cos(\chi)S_{HH} + i\sin(\chi)S_{HV}, i\sin(\chi)S_{VV} + \cos(\chi)S_{HV}]^T. \tag{3}$$

Here, it is assumed that the orientation angle of the elliptical wave is 0.

To enable a direct comparison between the RS-2 and RI-1 scenes, we simulate HP data from RS-2 data according to Equations (2) and (3). The simulated Stokes vector from the FP RS-2 data is calculated according to the method suggested in [5]. The reader is referred to [5] for additional theory of the HP mode.

As previously mentioned in [23], RI-1 circular right better matches simulated circular left from RS-2 on transmit. Our investigations corroborate these findings; by inspecting the fourth element of the Stokes vector we see clear indications of a sign reversal being necessary to obtain a basis equal to that of simulated HP RS-2. To the author's knowledge, there is no prior explanation to this left/right sign reversal but possible explanations are (1) different sign conventions as indicated in [23], and (2) the definition of the direction of the propagated wave is reversed when comparing the circular transmitted wave for RI-1 and the simulated circular transmitted wave from RS-2. To compensate for this sign reversal, we multiply the fourth element of the Stokes vector with minus one for RI-1. This sign reversal is also taken into consideration when changing both the transmitted and received basis to RR and RL for RI-1.

There exists several multipolarization features that can be extracted from the SAR data. Table 3 shows the features that are investigated. This table is split into two, where Table 3a describes the features analytically and Table 3b groups the features according to the groups defined in [9]. In this study the Stokes vector (see [5]) and the corresponding child parameters given in Table 3a are used. In addition, we also selected the four backscatter intensities, which are also located in Table 3a. The features in Table 3 are calculated from the RI-1 scenes, and from the simulated HP data for the

RS-2 scenes using both ellipticity angles of $\chi = -45°$ (perfect right-hand circular) and $\chi = -38°$ (right-hand elliptical). Some of these features are used previously in a study based on simulated HP data from RS-2 [6] and real HP data from RI-1 [11]. The selection of the features in our study is based on having a mix of both ratio-based and non ratio-based features, and testing features that are also from the five groups defined in [9]. In this study we follow the grouping of features suggested in [9], where a set of HP features were categorized into four groups based on their correlation to one another and one independent group. The groups defined in Geldsetzer et al. [9] corresponded to different scattering mechanisms. Table 3b shows the HP features sorted according to the grouping defined in Geldsetzer et al. [9], and the last column shows the information about the dominant scattering type that each group is sensitive to. For the σ_{RR} and σ_{RL} the basis of the receiver is changed to right- and left- hand circular. When calculating the σ_{RR} and σ_{RL} for the simulated HP data from RS-2 with an ellipticity angle of $-38°$, the transmitted wave is $-38°$ (right-hand elliptical), while the received basis is $\pm45°$ (perfect left- and right-hand circular).

The features in Group 1 respond to surface scattering, and the features that are in this group are q_0, q_3, σ_{RH}, σ_{RV}, and σ_{RL}. The σ_{RR} feature is categorized into Group 2 where depolarization due to volume scattering dominates. Further, $1 - m$, $\rho_{(RH,RV)}$, and $\gamma_{(RR,RL)}$ respond to depolarization likely due to multiscattering from rough surfaces, which is Group 3, while $\gamma_{(RH,RV)}$ is in Group 4 where it responds to polarization differences in resonant Bragg scattering and also in the Fresnel coefficients (see [24,25] for more information). Finally, the independent group, where the features are likely to give additional information that may be complementary to the other features [9]. The α_s is categorized into the independent group, and this feature is a function of the q_1, q_2, and q_3 from the Stokes vector. The α_s is an approximation to the α (from the H/α-decomposition), and it describes the dominant scattering mechanism [22]. In addition, the α_s is closely related to the ellipticity angle [26]. These groups are used in the discussion part in Section 4 when exploring the features ability to separate various sea ice types as well the correlation between RI-1 and RS-2.

In order to evaluate the separability between the sea ice types, the two sample Kolmogorov-Smirnov (K-S) test is used [27]. The K-S test, from here and out named the K-S distance, is based on the maximum difference between two cumulative distributions. The K-S distance gives values between 0 and 1, where a K-S distance close to 0 indicates that the two cumulative distributions are equal, while a value close to 1 indicates unequal cumulative distributions. Good separability between two given samples is achieved if K-S is above 0.9 [9]. In this study, the K-S distance is calculated for each of the investigated features between the sea ice types within each scene. Hence, we can identify which features manage to separate pairs of different sea ice types for each sensor in all the scene pairs.

To enable investigation of the correlation between the two sensors, the Spearman's rank correlation coefficient (r_s) is used (see [28] for additional information on Spearman's correlation). The Spearman's correlation coefficient is calculated between two profiles (from RI-1 and RS-2) that passes through the azimuth direction, this is done to avoid any incidence angle effects. The Spearman's correlation assesses monotonic relationship (linear or not) and is also less sensitive to strong outliers than the commonly used Pearson correlation. The Spearman's correlation gives values between -1 and 1, where values of ±1 imply full correlation, and no correlation for values corresponding to 0. In [29], the author classified the intervals of the correlation values obtained from Pearson correlation. Five classes were found, from "very weak" to "very strong". The same framework is utilized here when analysing the correlation values obtained from the Spearman's correlation coefficient.

Table 3. (a); an overview of the investigated hybrid-polarity (HP) features [5,9,26,30,31]. (b); the HP features sorted into groups. The features within a group have common scattering types that they are predominately sensitive to (see [9]).

(a)

HP Features

Name	Formula
Stokes vector	$\boldsymbol{q} = \begin{bmatrix} q_0 \\ q_1 \\ q_2 \\ q_3 \end{bmatrix} = \begin{bmatrix} \langle |S_{RH}|^2 + |S_{RV}|^2 \rangle \\ \langle |S_{RH}|^2 - |S_{RV}|^2 \rangle \\ 2\Re\langle (S_{RH} S_{RV}^\star) \rangle \\ -2\Im\langle (S_{RH} S_{RV}^\star) \rangle \end{bmatrix}$
Degree of polarization	$\mathrm{m} = \dfrac{\sqrt{q_1^2 + q_2^2 + q_3^2}}{q_0}$
α angle	$\alpha_s = \dfrac{1}{2} \tan^{-1}\left(\dfrac{\sqrt{q_1^2 + q_2^2}}{q_3} \right)$
Correlation coefficient	$\rho_{(RH,RV)} = \dfrac{|\langle S_{RH} S_{RV}^\star \rangle|}{\sqrt{\langle |S_{RH}|^2 \rangle \langle |S_{RV}|^2 \rangle}}$
Backscattered intensity coefficients	$\sigma_{RH}, \sigma_{RV}, \sigma_{RR}, \sigma_{RL}$
Ratio between RH and RV and circular ratio	$\gamma_{(RH,RV)} = \dfrac{\sigma_{RH}}{\sigma_{RV}}, \gamma_{(RR,RL)} = \dfrac{\sigma_{RR}}{\sigma_{RL}}$

(b)

Group Number	HP Features	Dominant Scattering Type
Group 1	σ_{RH} σ_{RV} σ_{RL} q_0 q_3	Surface scattering
Group 2	σ_{RR}	Depolarzation due to volume scattering
Group 3	$1 - m$ $\gamma_{(RR,RL)}$ $\rho_{(RH,RV)}$	Depolarization due to multiscattering from rough surfaces
Group 4	$\gamma_{(RH,RV)}$	Polarization differences in resonant Bragg scattering and also in the Fresnel coefficients.
Independent group	q_1 q_2 α_s	Might be complementary to other parameters

4. Results and Discussion

This section presents the noise analysis where the backscattered intensities from the regions of interest in the SAR scenes are compared to the NESZ for each of the two sensors. Further, the separability between the various sea ice types are investigated through the K-S distance, and the correlation between selected profiles through the scene pairs are presented.
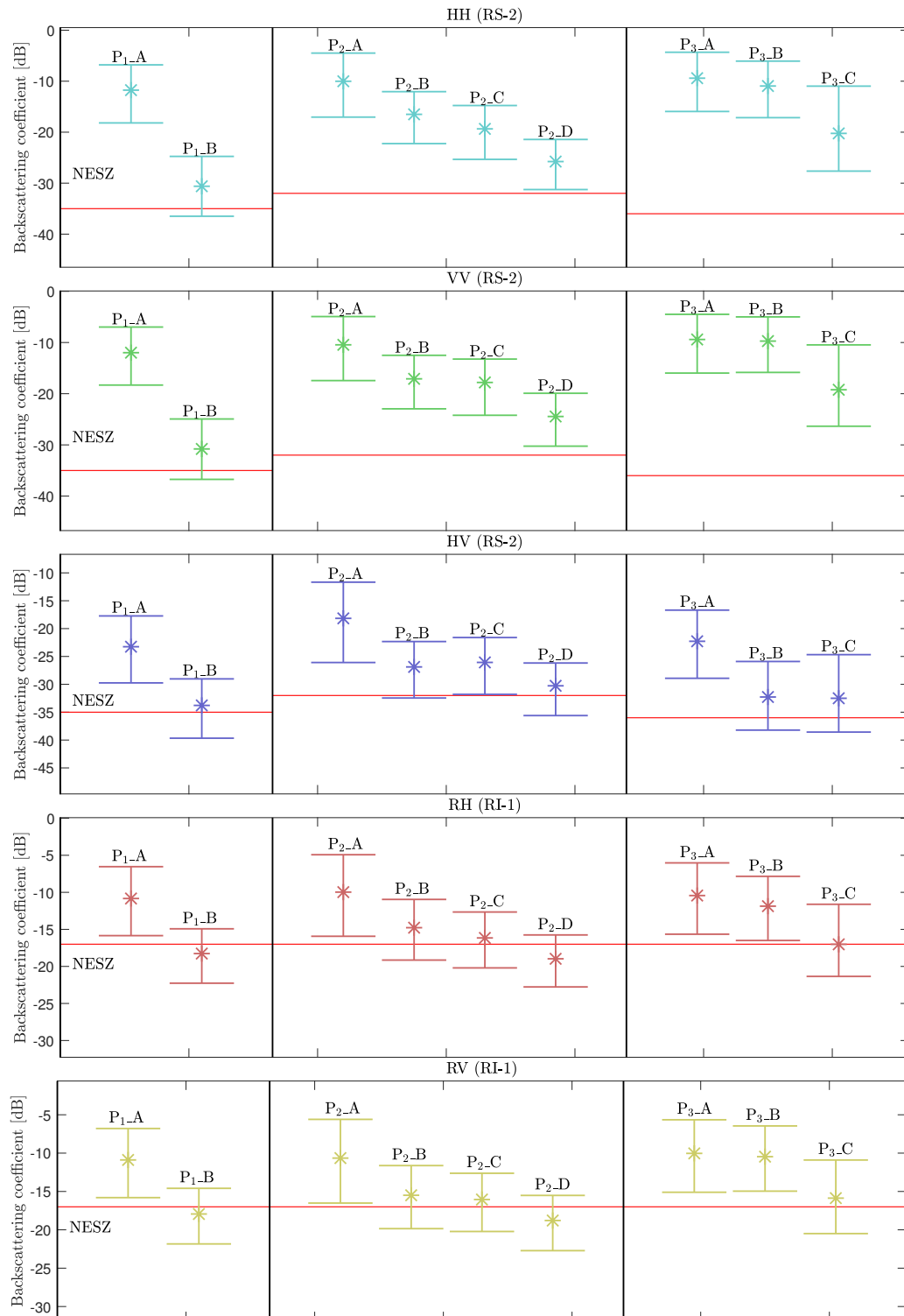
4.1. Noise Analysis

The returns from thin sea ice are low compared to other sea ice types (for example, ridges and multi-year ice), and the signal may be close to the noise floor, which introduce challenges when trying to separate different classes of thin sea ice [32]. The noise floor provided with the FRS-1 mode of RI-1 is given in [16] by a constant value of -17 dB. The noise floor of the fine quad-polarimetric SAR mode in RS-2 varies depending on the beam and incidence angle and is in the range -31.4 to -37.2 dB for the RS-2 scenes investigated in this study [17].

Figure 6 shows a signal-to-noise analysis of the ROIs representing various sea ice types we investigate. The 5th, 50th, and 95th percentiles of the HH, VV, and HV backscattering coefficients are calculated for each sea ice type in RS-2, and for the RH and RV backscattering coefficients for each sea ice type in RI-1. A star indicates the 50th percentile, and the horizontal continuous lines represent the 5th (bottom line) and 95th (top line) percentile for the backscattering coefficients. There are varying incidence angles in the three RS-2 scenes, which give various NESZ values for each of the sea ice types we investigate. Hence, the mean NESZ for each RS-2 scene is given in Figure 6. Across the copolarization backscattering coefficients of RS-2, only P_1_B has some values below the noise floor of RS-2. The sea ice types denoted by P_1_B, P_2_B, P_2_C, P_2_D, P_3_B, and P_3_C are either below or close to the noise floor in the HV backscattering coefficient in the RS-2 scenes.

Several of the sea ice types in the RI-1 scenes have pixels below or close to the noise floor, namely P_1_B, P_2_B, P_2_C, P_2_D, and P_3_C (see Table 2). Previous studies have indicated calibration issues related to the RI-1 sensor, and this might affect how the percentiles in Figure 6 are positioned above the NESZ. We will in Section 4.2 see better separability between some of the sea ice types for the RI-1 compared to RS-2. For example, the results in Section 4.2 show that features from RI-1 managed to separate P_2_B, P_2_C, and P_2_D, which are sea ice types that have backscattering values very close to the NESZ. Based on Figure 6, the signal-to-noise ratio is better for the RS-2 than for the RI-1.

4.2. Separability between the Sea Ice Types

The polarimetric feature values are calculated for each sea ice type for all the scene pairs, and an equal number of samples within two given ROIs representing two sea ice types are used as input to calculate the K-S distance. The results are presented in Figures 7–9. In these figures, the K-S distance values are given in a table, where values equal or above 0.9 are presented in bold, indicating good separability between two given sea ice types. The log-transformed version of the features are chosen when this increase the separability; these cases are indicated by "dB" after the feature name. The tables are separated into five sections, where each section corresponds to one of the five groups (see Table 3). These groups are used to link the separability between the various sea ice types obtained for a given feature to the scattering type dominating this group. For all figures, the values from the table are illustrated in a plot where the y-axis represents the K-S value (red dashed line for RI-1, green and blue line for simulated HP data from RS-2 with ellipticity angles of $\chi = -45°$ and $\chi = -38°$), and the x-axis is the polarimetric feature. Note, both ellipticity angles of $\chi = -45°$ and $\chi = -38°$ are present in the plots to show the effect of not having perfectly circular transmitted waves, while the table contains only the simulated HP with perfect circular on transmit. In the following, only the HP features from RI-1 and the simulated HP from RS-2 with perfect circular on transmits are discussed. The non-circularity property is discussed separately in Section 4.3 by considering the simulated HP systems with an ellipticity angle of $\chi = -38°$.

Figure 6. Signal-to-noise analysis of the backscattering intensity coefficients of the HH, VV, and HV for RS-2, and RH and RV for RI-1 for the investigated sea ice types. The 50th percentile is indicated by a star. The top and bottom horizontal continuous lines represent the 95th percentile and 5th percentile for the intensities, respectively. The red line represents NESZ. The y-axis represents the backscattering intensity coefficient, while the different sea ice types (i.e., ROIs) are aligned along the x-axis sorted by scene pair number.

4.2.1. Pair #1

The table in Figure 7 contains K-S values between the two sea ice types in P_1 (FYI and grease/frazil ice). Several of the features extracted from the RI-1 and the overlapping RS-2 scenes show high separability between P_1_A and P_1_B. $\gamma_{(RH,RV)}$, q_1, and α_s are the features with the lowest K-S values for the RI-1 scene, and $\gamma_{(RH,RV)}$, q_1, q_2, and α_s are the features with the lowest K-S values for RS-2. For the features in Groups 1 and 2, the separability of the sea ice types is almost identical for RI-1 and RS-2, whereas the features in Group 3 show higher separability between the two sea ice types using the RI-1 data. The feature in Group 4 show poorer separation (lower K-S distance) between the two sea ice types.
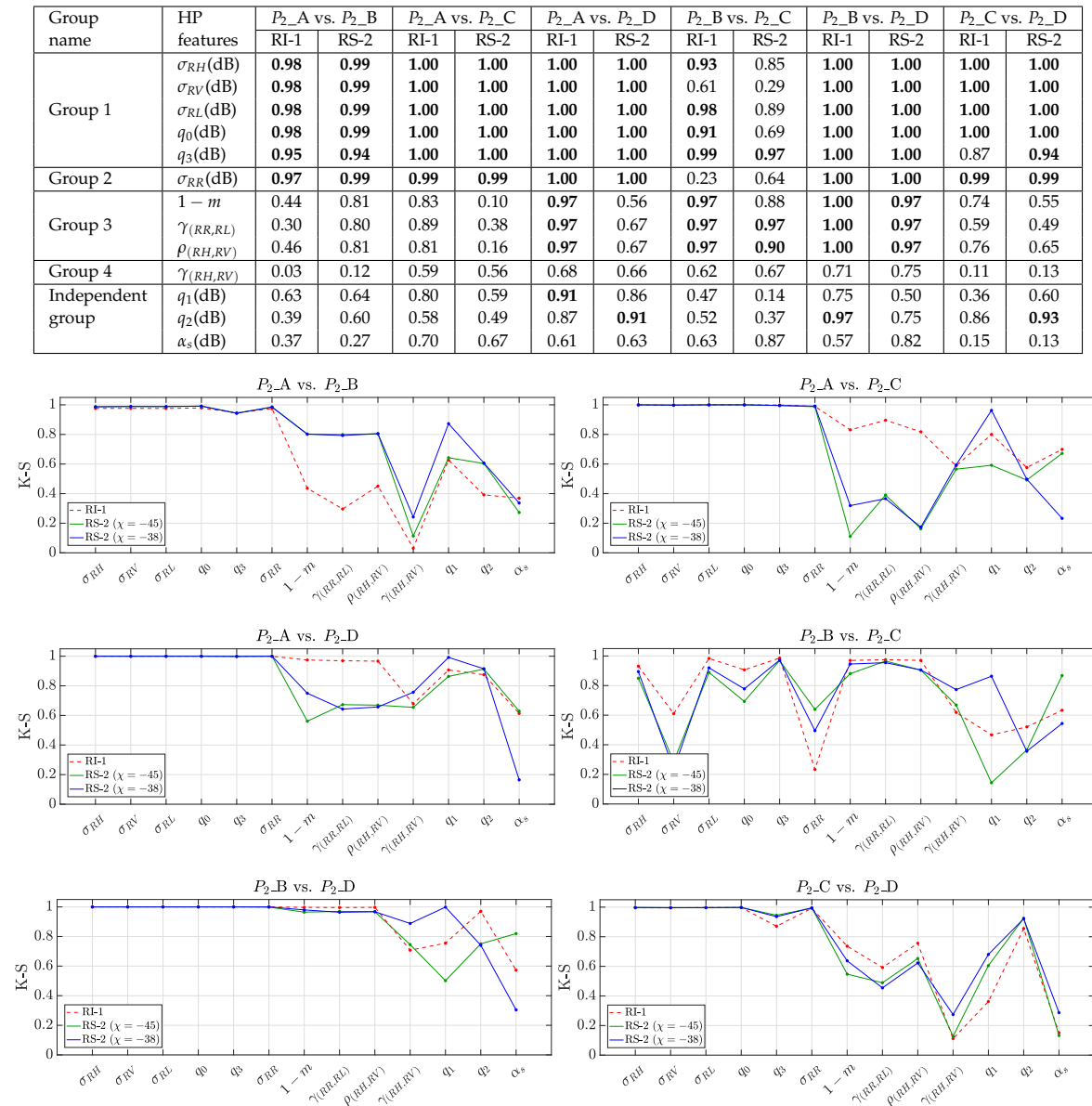
Group name	HP features	P_1_A vs. P_1_B RI-1	P_1_A vs. P_1_B RS-2
Group 1	σ_{RH}(dB)	**0.98**	**0.99**
	σ_{RV}(dB)	**0.99**	**0.99**
	σ_{RL}(dB)	**0.99**	**0.99**
	q_0(dB)	**0.98**	**0.99**
	q_3(dB)	**0.99**	**0.99**
Group 2	σ_{RR}(dB)	**0.98**	**0.98**
Group 3	$1 - m$	**0.99**	**0.90**
	$\gamma_{(RR,RL)}$	**0.99**	**0.91**
	$\rho_{(RH,RV)}$	**0.99**	**0.90**
Group 4	$\gamma_{(RH,RV)}$	0.38	0.06
Independent group	q_1(dB)	0.58	0.84
	q_2(dB)	**0.99**	0.86
	α_s(dB)	0.80	0.82
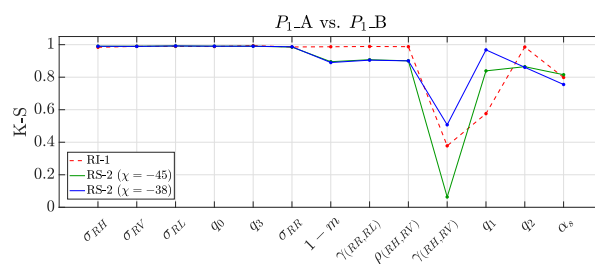
Figure 7. Left panel; a table containing the Kolmogorov-Smirnov (K-S) separability values between the two sea ice types in P_1. The first column shows the groups as described in Table 3. The values greater than 0.9 are in bold. Right panel; the corresponding values are shown in the plot for the two sea ice types, where the y-axis shows the K-S values calculated for the two sea ice types (i.e., ROIs) (red for the RI-1 features and green (blue) for the RS-2 features with an ellipticity angle of $\chi = -45°$ ($-38°$)), while the x-axis shows the corresponding features. Note that only the K-S values for RI-1 features and the RS-2 features using an ellipticity angle of $\chi = -45°$ is shown in the table.

4.2.2. Pair #2

Figure 8 contains K-S values between the four distinct sea ice types in P_2. Here, all the sea ice types are possible to separate according to the threshold set for the K-S (K-S > 0.9). The features yielding K-S values above or close to 0.9 between the four sea ice types using the RI-1 scene are σ_{RH}, σ_{RL}, q_0, and q_3. For the RS-2 scenes, features producing K-S > 0.9 are σ_{RH}, σ_{RL}, and q_3. The features in Groups 1 and 2 give high K-S values for all the pairs of the different sea ice types except between P_2_B and P_2_C. Recall from Table 2, that P_2_B and P_2_C are defined as flooded FYI and nilas with snow cover. P_2_C and P_2_D are the sea ice types (nilas and leads) with the lowest backscattering level (see Figure 6), and the features giving maximum separability between the two belong to Groups 1 and 2 for both RI-1 and RS-2. The features in Group 3 show different separability trends for the two sensors, while for the remaining features the separability of the paired sea ice types between RS-2 and RI-1 are very similar. The same observation for Group 3 is true for P_1. This might be related to the varying noise level in the two sensors, since features in Group 3 are sensitive to the depolarization effects. This difference might thus be because of RI-1 having higher noise floor than to RS-2. It is clear from this figure that the features in Group 4 and the independent group (last row in the table) show poor separability between the sea ice types using both RS-2 and RI-1 with minor exceptions.

Group name	HP features	P_2_A vs. P_2_B		P_2_A vs. P_2_C		P_2_A vs. P_2_D		P_2_B vs. P_2_C		P_2_B vs. P_2_D		P_2_C vs. P_2_D	
		RI-1	RS-2	RI-1	RS-2	RI-1	RS-2	RI-1	RS-2	RI-1	RS-2	RI-1	RS-2
Group 1	σ_{RH}(dB)	**0.98**	**0.99**	**1.00**	**1.00**	**1.00**	**1.00**	**0.93**	0.85	**1.00**	**1.00**	**1.00**	**1.00**
	σ_{RV}(dB)	**0.98**	**0.99**	**1.00**	**1.00**	**1.00**	**1.00**	0.61	0.29	**1.00**	**1.00**	**1.00**	**1.00**
	σ_{RL}(dB)	**0.98**	**0.99**	**1.00**	**1.00**	**1.00**	**1.00**	**0.98**	0.89	**1.00**	**1.00**	**1.00**	**1.00**
	q_0(dB)	**0.98**	**0.99**	**1.00**	**1.00**	**1.00**	**1.00**	**0.91**	0.69	**1.00**	**1.00**	**1.00**	**1.00**
	q_3(dB)	**0.95**	**0.94**	**1.00**	**1.00**	**1.00**	**1.00**	**0.99**	**0.97**	**1.00**	**1.00**	0.87	**0.94**
Group 2	σ_{RR}(dB)	**0.97**	**0.99**	**0.99**	**0.99**	**1.00**	**1.00**	0.23	0.64	**1.00**	**1.00**	**0.99**	**0.99**
Group 3	$1-m$	0.44	0.81	0.83	0.10	**0.97**	0.56	**0.97**	0.88	**1.00**	**0.97**	0.74	0.55
	$\gamma_{(RR,RL)}$	0.30	0.80	0.89	0.38	**0.97**	0.67	**0.97**	**0.97**	**1.00**	**0.97**	0.59	0.49
	$\rho_{(RH,RV)}$	0.46	0.81	0.81	0.16	**0.97**	0.67	**0.97**	**0.90**	**1.00**	**0.97**	0.76	0.65
Group 4	$\gamma_{(RH,RV)}$	0.03	0.12	0.59	0.56	0.68	0.66	0.62	0.67	0.71	0.75	0.11	0.13
Independent group	q_1(dB)	0.63	0.64	0.80	0.59	**0.91**	0.86	0.47	0.14	0.75	0.50	0.36	0.60
	q_2(dB)	0.39	0.60	0.58	0.49	0.87	**0.91**	0.52	0.37	**0.97**	0.75	0.86	**0.93**
	α_s(dB)	0.37	0.27	0.70	0.67	0.61	0.63	0.63	0.87	0.57	0.82	0.15	0.13

Figure 8. Top panel; a table containing the K-S values between all combinations of paired sea ice types in P_2. The first column shows groups as described in Table 3. The values greater than 0.9 are in bold. Bottom panels; the corresponding values are shown in the plots, where the y-axis shows the K-S values calculated for each of the paired sea ice types (i.e., ROIs) (red for the RI-1 features and green (blue) for the RS-2 features with an ellipticity angle of $\chi = -45°$ ($-38°$)), while the x-axis shows the corresponding features. Note that only the K-S values for RI-1 features and the RS-2 features using an ellipticity angle of $\chi = -45°$ is shown in the table.

4.2.3. Pair #3

The K-S values between the classes evaluated from P_3 are given in Figure 9. The separability values between P_3_A and P_3_C (the brightest and the darkest regions) are highest in Groups 1 and 2, where features responding to strong surface scattering and depolarization due to volume scattering are located. Note that the features in Groups 1 and 2 are all non ratio-based features. None of the RI-1 features give a K-S value above 0.9 when separating P_3_A and P_3_B, whereas all the features in Groups 2, 3, and 4 gives K-S values above 0.9 for the RS-2 scenes. These are the scenes with lowest incidence angle and sea ice with a new fresh snow layer. P_1_A and P_1_B were categorized as FYI and grease ice (see Table 2), while P_3_A and P_3_B were identified as the same ice types, but with a new

fresh snow layer. It is interesting that the features in Group 1 (features dominated by surface scattering) show high separability values for the sea ice types in P_1, but the separation values decreases when a snow layer covers the similar sea ice types in P_3 (see Table 2). This corroborates the findings in [33], where the importance of volume and multiple scattering will increase with snow thickness. Therefore, the features in Group 1, where surface scattering dominates, show poor separability between P_3_A and P_3_B (FYI and grease ice with a fresh snow layer).

Group name	HP features	P_3_A vs. P_3_B		P_3_A vs. P_3_C		P_3_B vs. P_3_C	
		RI-1	RS-2	RI-1	RS-2	RI-1	RS-2
Group 1	σ_{RH}(dB)	0.66	0.74	**1.00**	**0.98**	**0.93**	**0.90**
	σ_{RV}(dB)	0.30	0.31	**0.99**	**0.98**	**0.98**	**0.96**
	σ_{RL}(dB)	0.36	0.37	**0.99**	**0.98**	**0.98**	**0.95**
	q_0(dB)	0.43	0.57	**1.00**	**0.98**	**0.97**	**0.94**
	q_3(dB)	0.16	0.10	**0.98**	**0.97**	**0.99**	**0.97**
Group 2	σ_{RR}(dB)	0.86	**0.97**	**0.99**	**0.95**	0.85	0.27
Group 3	$1-m$	0.78	**0.97**	0.85	0.34	**0.98**	**0.96**
	$\gamma_{(RR,RL)}$	0.78	**0.96**	0.86	0.38	**0.98**	**0.96**
	$\rho_{(RH,RV)}$	0.72	**0.97**	0.87	0.36	**0.98**	**0.96**
Group 4	$\gamma_{(RH,RV)}$	0.85	0.81	0.53	0.44	0.43	0.40
Independent group	q_1(dB)	0.71	0.50	0.31	0.49	**0.92**	**0.90**
	q_2(dB)	0.22	0.39	**0.96**	0.60	**0.95**	0.34
	α_s(dB)	0.13	0.29	0.44	0.42	0.54	0.46
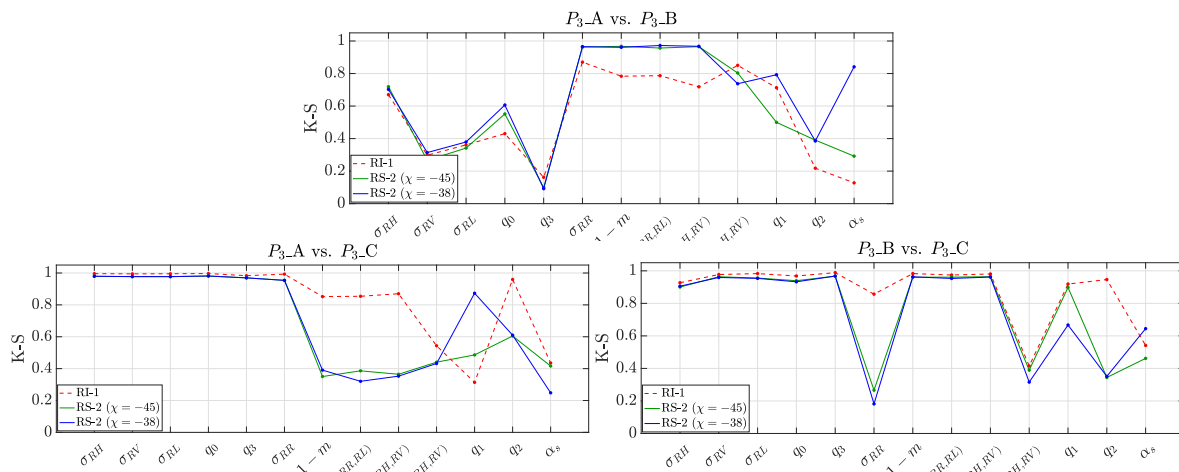
Figure 9. Top panel; a table containing the K-S values between all combinations of paired sea ice types in P_3. The first column shows groups as described in Table 3. The values greater than 0.9 are in bold. Bottom panels; the corresponding values are shown in the plots, where the y-axis shows the K-S values calculated for each of the paired sea ice types (i.e., ROIs) (red for the RI-1 features and green (blue) for the RS-2 features with an ellipticity angle of $\chi = -45°$ ($-38°$)), while the x-axis shows the corresponding features. Note that only the K-S values for RI-1 features and the RS-2 features using an ellipticity angle of $\chi = -45°$ is shown in the table.

4.2.4. Summary

From Figures 7–9, the separability values obtained from RS-2 and RI-1 features are similar across most of the pairwise combinations of the available sea ice types. However, the RI-1 features have slightly higher K-S values compared to the RS-2 features for the majority of the paired sea ice types. The majority of the panels in Figures 7–9 (7 out of 10) show differences for Group 3 between RI-1 and RS-2. One possible explanation for this behaviour might be the different NESZ for the two sensors. When increasing the additive noise of the simulated HP from the RS-2 products, the features in Group 3 were the ones most affected. This effect was confirmed by comparing the K-S values between the simulated HP data with and without an increase in the additive noise term. Note that the features in Group 4 are all ratio-based features.

In Figure 6, a higher NESZ is given for the investigated modes for the RI-1 products compared to the NESZ of RS-2. The RI-1 features still manage to separate the sea ice types that have backscattering coefficients close to the NESZ, which might indicate that the NESZ is lower than stated in the product description of RI-1 (as already highlighted by the calibration issue of RI-1 in [14]). In addition, the RI-1 products had finer resolution than the RS-2 product, and thus more averaging is performed for the RI-1 products to obtain the same ground resolution on the projected common grid. More averaging will reduce the speckle and increase class interpretability resulting in increased separability between the different sea ice types. There is also a trend in which group of features providing high separability as well as obtaining relative equal K-S values for the RI-1 and RS-2. Overall, the group of features that show equal separability between the sea ice types amongst all the scene pairs are Group 1 (the non ratio-based features), while amongst all the scene pairs the features in the independent group show the highest deviation between the K-S values obtained from RS-2 and RI-1. Evaluating all the K-S values together, the features that provide the overall highest separability are from Groups 1, 2, and 3, while the features that show poor separability are from Group 4 and the independent group.

4.3. The Non-Circularity Property

When simulating HP data from FP data using RS-2, we simulate perfect circular polarization on transmit. At the target, there might be an uncertainty associated with the actual transmitted wave, due to the non-circularity of a HP system in general, which was pointed out in [20] and tested in [14] for RI-1. These uncertainties are associated with, for example, propagation effects, transmitter, and antenna performance [34]. Therefore, a simulation on $\chi = -38°$ (right-hand elliptical on transmit) from the RS-2 data was performed and compared to the RI-1 features and the simulated perfect circular HP from RS-2. The results are shown in Figures 7–9, where the blue line is the HP with $\chi = -38°$, while the green line is $\chi = -45°$. It is clear that the separability between the sea ice types are mostly similar for both $\chi = -38°$ and $\chi = -45°$. However, three features seem to be affected by the non-circularity property, these are q_1, $\gamma_{(RH,RV)}$, and α_s. Using q_1 and $\gamma_{(RH,RV)}$ the overall separability was higher for $\chi = -38°$ between the majority of the paired sea ice types. However, using α_s the overall separability was higher for $\chi = -45°$ between the majority of the paired sea ice types. All the features in Groups 1, 2, and 3 are stable when it comes to the ability to separate the various sea ice types for all the scene pairs, while unstable for Group 4 and the independent group, with the exception of q_2. This set of features (Group 4 and the independent group) is also found to show poor correlation between RS-2 and RI-1, which is discussed in Section 4.4.

4.4. Correlation between RS-2 and RI-1

The correlation between the two sensors are here evaluated through the Spearman's correlation coefficient (r_s) of three profiles in each scene pair shown in Figures 2–4. Three profiles are used to capture the variations along range direction in each scene pair. The three profiles are along azimuth direction, and the width of the profiles are the along range direction. The width of each profile is approximately 50 pixels. The mean along range direction is taken for each profile, leaving the resulting mean profile to be one pixel wide. Further, the correlation for a given feature extracted from RI-1 and RS-2 is calculated for each profile. The Spearman's correlation coefficients are shown in Table 4, where correlation values above 0.8 (strong to very strong correlation) are colored red. Note, log-transformed versions of the features are chosen when this increases the correlation; these cases are indicated by "dB" after the feature name.

For the three profiles in P_1 and P_2; a strong to very strong correlation is observed for the majority of the features in Groups 1 and 2 (non ratio-based features), while the majority of the ratio-based features and q_1 and q_2 fall in the very weak to moderate correlation categories (see discussion on the Spearman's correlation coefficient in Section 3). In addition, stronger r_s is found for the profiles in P_2 compared to the profiles in P_1. The r_s values for the profiles in P_3 are given in the last three columns in Table 3. Here, a strong to very strong correlation is observed for the features in Group 3. Note that the

features in Group 1 gave a strong to very strong correlation in the three profiles in P_1 and P_2. This trend is not observed for the three profiles in P_3.

The profiles in P_3 are the ones which resulted in the lowest correlation amongst all the profiles. Compared to P_1 and P_2, the scenes in P_3 contain sea ice (grease ice and FYI) covered with a fresh snow layer. In addition the scenes in P_3 had the lowest incidence angle (22.5°–25.3°) compared to the other scene pairs. Further the variations in the r_s values across the three profiles within each scene pair are small.

Comparing the results from Figures 7 and 8 and the r_s in Table 4 it is possible to identify a trend between high separability between the investigated sea ice types and the strong Spearman's correlation for Groups 1 and 2. This is only true for scene pairs P_1 and P_2. The features that give mostly strong correlation in all scene pairs are σ_{RH}, q_0, and σ_{RR}. These are features from Groups 1 and 2. Note that σ_{RH}, q_0, and σ_{RR} had also high K-S distances between the majority of the sea ice types investigated. The remaining features show varying correlation coefficients across the scene pairs.

Table 4. The Spearman's correlation coefficient (r_s) (absolute value) between RI-1 and RS-2 for the three profiles in each pair (seen Figure 5). The r_s values that are above 0.8 (strong correlation) are colored red. The first column shows the groups as described in Table 3.

Group			P₁			P₂			P₃		
Name	**Profile #**	**1**	**2**	**3**	**1**	**2**	**3**	**1**	**2**	**3**	
	σ_{RH} (dB)	0.80	0.88	0.82	0.90	0.93	0.96	0.70	0.85	0.89	
	σ_{RV} (dB)	0.80	0.88	0.82	0.91	0.94	0.96	0.57	0.68	0.74	
Group 1	σ_{RL} (dB)	0.80	0.88	0.83	0.90	0.94	0.96	0.59	0.70	0.78	
	q_0 (dB)	0.83	0.88	0.83	0.90	0.92	0.94	0.65	0.80	0.86	
	q_3 (dB)	0.84	0.87	0.83	0.75	0.90	0.92	0.64	0.61	0.61	
Group 2	σ_{RR} (dB)	0.79	0.87	0.81	0.92	0.94	0.95	0.77	0.92	0.90	
	$1-m$	0.77	0.83	0.76	0.63	0.70	0.63	0.86	0.90	0.84	
Group 3	$\gamma_{(RR,RL)}$	0.79	0.84	0.77	0.66	0.68	0.68	0.84	0.88	0.84	
	$\rho_{(RH,RV)}$	0.78	0.84	0.76	0.64	0.71	0.65	0.86	0.89	0.84	
Group 4	$\gamma_{(RH,RV)}$	0.06	0.14	0.16	0.16	0.27	0.51	0.59	0.79	0.81	
Independent group	q_1 (dB)	0.65	0.76	0.66	0.48	0.64	0.84	0.56	0.72	0.70	
	q_2 (dB)	0.75	0.84	0.78	0.37	0.34	0.73	0.17	0.44	0.45	
	α_s (dB)	0.68	0.70	0.63	0.22	0.14	0.58	0.06	0.05	0.16	

5. Conclusions

In this study we investigated the relationship between a real and a simulated HP system in three overlapping pairs of RI-1 and RS-2 scenes covering Arctic sea ice, with relatively small time difference between acquisitions and similar incidence angles. Thirteen HP features are evaluated both from real HP data (RI-1) and simulated HP data from RS-2.

Several polarimetric features from the two groups where surface scattering and depolarization due to volume scattering dominates showed great potential for separating various sea ice types based on the K-S values. We conclude that the HP mode of RI-1 and the simulated HP mode of RS-2 show comparable performance in separating the sea ice types. Amongst all the scene pairs, the features in the independent group had the highest deviation between the K-S values obtained from RS-2 and RI-1. Recall, the independent group contains features that likely give additional information that may be complementary to the groups sensitive to various scattering mechanisms.

The features that show poor separability are from the group that was sensitive to polarization differences in resonant Bragg scattering and also in the Fresnel coefficients, and from the independent group.

The NESZ provided with RI-1 is given as a constant value of −17 dB, and the backscattering values from some sea ice types were close to and sometimes below this value. We discovered a high separability between sea ice types that had backscattering values close to NESZ, which might indicate that the RI-1 quality in terms of NESZ is better than previously reported.

Three polarimetric features seem to be affected by not having a perfect circular wave on transmit, these are q_1, $\gamma_{(RH,RV)}$, and α_s. However, the separability between the different sea ice types using features from the groups where surface scattering and depolarization due to multiple/volume scattering dominates are similar for both ellipticity angles of $\chi = -38°$ and $\chi = -45°$. We therefore conclude that having a more elliptical wave on transmit will not affect the separability of the investigated sea ice types given that the correct features are selected.

For two of the three scene pairs (P_1 and P_2) we discovered a high Spearman's correlation between the profiles using the polarimetric features from RI-1 and RS-2 that are in groups where surface scattering and depolarization due to volume scattering dominates. For P_3 the features sensitive to depolarization due to volume and multiple scattering showed high correlation. These results might be explained by a snow layer contributing to more volume scattering in P_3 (see e.g., [33]), and our results indicate that the features that are sensitive to volume/multiple scattering give higher correlation between the two sensors. The Spearman's correlation for the features extracted from RS-2 and RI-1 profiles were relatively consistent across each scene pair. However, no individual feature showed strong to very strong correlation across all three scene pairs. Although the features σ_{RH}, q_0, and σ_{RR} showed strong to very strong correlation across all three scene pairs expect for 1–2 profiles which had moderate correlations between the sensors. Note, these features also gave high separability values between the majority of the paired ROIs, and were not so affected by the non-circularity property. Therefore, the features σ_{RH}, q_0, and σ_{RR} are recommended to use when the FRS-1 mode of RI-1 and RS-2 data are combined for change detection purposes or for increasing the coverage when monitoring the surface.

Future studies will include investigation of the the non-circularity property of the transmitted wave for a larger set of multipolarization features. We also wish to identify the reasons why some polarimetric features are affected by the non-circularity property and some are not.

Author Contributions: Martine M. Espeseth, Camilla Brekke, and A. Malin Johansson were all involved in the study design and writing of this paper. Martine M. Espeseth analyzed the data and made the figures and tables. Martine M. Espeseth and A. Malin Johansson ordered the satellite acquisitions. A. Malin Johansson collected the in-situ sea ice and accompanying measurements (in part with the Norwegian Polar Institute).

Conflicts of Interest: The authors declare no conflict of interest.

References

1. Maillard, P.; Clausi, D.A.; Deng, H. Operational Map-Guided Classification of SAR Sea Ice Imagery. *IEEE Trans. Geosci. Remote Sens.* **2005**, *43*, 2940–2951.

2. Walker, N.P.; Partington, K.C.; Woert, M.L.V.; Street, T.L.T. Arctic Sea Ice Type and Concentration Mapping Using Passive and Active Microwave Sensors. *IEEE Trans. Geosci. Remote Sens.* **2006**, *44*, 3574–3584.

3. Moen, M.A.N.; Doulgeris, A.P.; Anfinsen, S.N.; Renner, A.H.H.; Hughes, N.; Gerland, S.; Eltoft, T. Comparison of feature based segmentation of full polarimetric SAR satellite sea ice images with manually drawn ice charts. *Cryosphere* **2013**, *7*, 1693–1705.

4. Moen, M.A.N.; Anfinsen, S.N.; Doulgeris, A.P.; Renner, A.H.H.; Gerland, S. Assessing polarimetric SAR sea-ice classifications using consecutive day images. *Ann. Glaciol.* **2015**, *56*, 285–294.

5. Raney, R.K. Hybrid-Polarity SAR Architecture. *IEEE Trans. Geosci. Remote Sens.* **2007**, *45*, 3397–3404.

6. Dabboor, M.; Geldsetzer, T. Towards sea ice classification using simulated RADARSAT Constellation Mission compact polarimetric SAR imagery. *Remote Sens. Environ.* **2014**, *140*, 189–195.

7. Dabboor, M.; Geldsetzer, T. On the Classification of Sea Ice Types using Simulated Radarsat Constellation Mission (RCM) Compact Polarimetric SAR Parameters. In Proceedings of the ASPRS 2014 Annual Conference, Louisville, Kentucky, 23–28 March 2014.

8. Li, H.; Perrie, W. Sea Ice Characterization and Classification Using Hybrid Polarimetry SAR. *IEEE J. Sel. Top. Appl. Earth Obs. Remote Sens.* **2016**, *9*, 4998–5010.

9. Geldsetzer, T.; Arkett, M.; Zagon, T.; Charbonneau, F.; Yackel, J.J.; Scharien, T.K. All-Season Compact-Polarimetry C-band SAR Observations of Sea Ice. *Can. J. Remote Sens.* **2015**, *41*, 485–504.

10. Xi, Z.; Jie, Z.; Meijie, L.; Junmin, M. Assessment of C-band compact polarimetry SAR for sea ice classification. *Acta Oceanol. Sin.* **2016**, *35*, 79–88.

11. Singha, S.; Ressel, R. Arctic Sea Ice Characterization Using RISAT-1 Compact-Pol SAR Imagery and Feature Evaluation: A Case Study Over Northeast Greenland. *IEEE J. Sel. Top. Appl. Earth Obs. Remote Sens.* **2017**, *10*, 3504–3514.

12. Souyris, J.C.; Imbo, P.; Fjortoft, R.; Mingot, S.; Lee, J.S. Compact polarimetry based on symmetry properties of geophysical media: the *pi*/4 mode. *IEEE Trans. Geosci. Remote Sens.* **2005**, *43*, 634–646.

13. Espeseth, M.M.; Brekke, C.; Anfinsen, S.N. Hybrid-Polarity and Reconstruction Methods for Sea Ice With L- and C-Band SAR. *IEEE Geosci. Remote Sens. Lett.* **2016**, *13*, 467–471.

14. Rao, Y.S.; Meadows, P.; Kumar, V. Evaluation of RISAT-1 compact polarization data for calibration. In Proceedings of the 2016 IEEE International Geoscience and Remote Sensing Symposium (IGARSS), Beijing, China, 10–15 July 2016; pp. 3250–3253.

15. Eriksson, L.E.B.; Borenäs, K.; Dierking, W.; Berg, A.; Santoro, M.; Pemberton, P.; Lindh, H.; Karlson, B. Evaluation of new spaceborne SAR sensors for sea-ice monitoring in the Baltic Sea. *Can. J. Remote Sens.* **2010**, *36*, 56–73.

16. Misra, T.; Rana, S.S.; Desai, N.M.; Dave, D.B.; Rajeevjyoti; Arora, R.K.; Rao, C.V.N.; Bakori, B.V.; Neelakantan, R.; Vachchani, J.G. Synthetic Aperture Radar payload on-board RISAT-1: Configuration, technology and performance. *Curr. Sci.* **2013**, *104*, 446–461.

17. Slade, B. *Radarsat-2 Product Description*; MacDonald, Dettwiler and Associates Ltd.: Rickmond, BC, USA, 2011.

18. Oliver, C.; Quegan, S. *Understanding Synthetic Aperture Radar Images*; SciTech Publishing Inc.: Raleigh, NC, USA, 2004.

19. Drinkwater, M. Airborne and Satellite SAR Investigations of Sea-Ice Surface Characteristics. In *Oceanographic Applications of Remote Sensing*; CRC Press: Boca Raton, FL, USA, 1995; Chapter IV-A-3, pp. 339–357.

20. Touzi, R.; Charbonneau, F. Requirements on the calibration of Hybrid-Compact SAR. In Proceedings of the 2016 IEEE International Geoscience and Remote Sensing Symposium (IGARSS), Quebec City, QC, Canada, 13–18 July 2014; pp. 1109–1112.

21. Stutzman, W.L.; Thiele, G.A. *Antenna Theory and Design*; John Wiley and Sons Inc.: Hoboken, NJ, USA, 1981.

22. Lee, J.S.; Pottier, E. Polarimetric Radar Imaging: from basic to applications, In *Optical Science and Engineering*; CRC Press Taylor and Francis Group: Abingdon, UK, 2009.

23. Kumar, V.; Rao, Y.S. Comparative analysis of RISAT-1 and simulated RADARSAT-2 hybrid polarimetric SAR data for different land features. In Proceedings of the The International Archives of the Photogrammetry, Remote Sensing and Spatial Information Sciences, ISPRS Technical Commission VIII Symposium, Hyderabad, India, 7–12 December 2014; Volume XL-8.

24. Zhang, X.; Dierking, W.; Zhang, J.; Meng, J.; Lang, H. Retrieval of the thickness of undeformed sea ice from simulated C-band compact polarimetric SAR images. *Cryosphere* **2016**, *10*, 1529–1545.

25. Cloude, S.R. *Polarisation Applications in Remote Sensing*; Oxford University Press Inc.: New York, NY, USA, 2010; pp. 125–129.

26. Cloude, S.R.; Goodenough, D.; Chen, H. Compact Decomposition Theory. *IEEE Trans. Geosci. Remote Sens.* **2012**, *9*, 28–32.

27. Massry, F.J., Jr. The Kolmogorov-Smirnov Test for Goodness of Fit. *J. Am. Stat. Assoc.* **1951**, *46*, 68–78.

28. Corder, G.W.; Foreman, D.I. *Nonparametric Statistics for Non-Statisticians: A Step-by-Step Approach*; Wiley: Hoboken, NJ, USA, 2009.

29. Evans, J.D. *Straightforward Statistics for the Behavioral Sciences*; Brooks/Cole Publishing Company, The University of California: Baltimore, MD, USA, 1996.

30. Charbonneau, F.J.; Brisco, B.; Raney, R.K.; McNairn, H.; Liu, C.; Vachon, P.W.; Shang, J.; DeAbreu, R.; Champagne, C.; Merzouki, A.; Geldsetzer, T. Compact Polarimetry Overview and Applications Assessment. *Can. J. Remote Sens.* **2010**, *36*, 298–315.

31. Dabboor, M.; Howell, S.; Shokr, M.; Yackel, J. The Jeffries-Matusita distance for the case of complex Wishart distribution as a separability criterion for fully polarimetric SAR data. *Int. J. Remote Sens.* **2014**, *35*, 6859–6873.

32. Dierking, W. Mapping of Different Sea Ice Regimes Using Images From Sentinel-1 and ALOS Synthetic Aperture Radar. *IEEE Trans. Geosci. Remote Sens.* **2010**, *48*, 1045–1058.

33. Gill, J.P.S.; Geldsetzer, T.; Fuller, M.C. Sensitivity of C-band synthetic aperture radar polarimetric parameters to snow thickness over landfast smooth first-year sea ice. *Remote Sens. Environ.* **2015**, *166*, 34–49.

34. Sabry, R.; Vachon, P.W. A Unified Framework for General Compact and Quad Polarimetric SAR Data and Imagery Analysis. *IEEE Trans. Geosci. Remote Sens.* **2014**, *52*, 582–602.